Nano Research

ISSN 1998-0124 CN 11-5974/O4
https://doi.org/10.1007/s12274-023-6022-2

Research Article

Two-dimensional atomically thin Pt layers on MXenes: The role of electronic effects during catalytic dehydrogenation of ethane and propane

Zhe Li[1,§], Tobias K. Misicko[2,§], Fan Yang[1,§], Xiaopeng Liu[1], Zhenwei Wu[3], Xiaoyang Gao[2], Tao Ma[4], Jeffrey T. Miller[3], Daniela S. Mainardi[2], Collin D. Wick[5], Zhenhua Zeng[3] (✉), Yang Xiao[2] (✉), and Yue Wu[1] (✉)

[1] *Department of Chemical and Biological Engineering, Iowa State University, 618 Bissell Road, Ames, IA 50011, USA*
[2] *Institute for Micromanufacturing, Louisiana Tech University, 505 Tech Drive, Ruston, LA 71272, USA*
[3] *Davidson School of Chemical Engineering, Purdue University, 480 Stadium Mall Drive, West Lafayette, IN 47907, USA*
[4] *Michigan Center for Materials Characterization, University of Michigan, 2800 Plymouth Rd, Ann Arbor MI 48109, USA*
[5] *College of Engineering and Science, Louisiana Tech University, Ruston, LA 71272, USA*
[§] *Zhe Li, Tobias K. Misicko, and Fan Yang contributed equally to this work.*

Received: 28 May 2023 / **Revised:** 18 July 2023 / **Accepted:** 19 July 2023

ABSTRACT

Atomically thin Pt nanolayers were synthesized on the surface of Mo_2TiC_2 MXenes and used for the catalytic dehydrogenation of ethane and propane into ethylene and propylene, two important chemicals for the petrochemical industry. As compared with Pt nanoparticles, the atomically thin Pt nanolayer catalyst showed superior coke-resistance (no deactivation for 24 h), high activity (turnover frequencies (TOFs) of 0.4–1.2 s^{-1}), and selectivity (> 95%) toward ethylene and propylene. The unique Pt nanolayer has a similar geometric surface to Pt nanoparticles, enabling the investigations of the electronic effect on the catalytic performance, where the geometric effect is negligible. It is found that the electronic effect plays a critical role in dehydrogenative product selectivity and catalyst stability. The metal–support interaction is found dependent on the substrate and metal components, providing wide opportunities to explore high-performance MXene-supported metallic catalysts.

KEYWORDS

MXene, catalysis, alkane, dehydrogenation, nanolayers

1 Introduction

Ethylene (C_2H_4) and propylene (C_3H_6) are the first and second most important platform chemicals in the petrochemical industry. They have been traditionally produced via steam cracking of short-chain hydrocarbons (such as naphtha) and fluid catalytic cracking (FCC) of long-chain hydrocarbons (such as heavy gas oil), both of which consume a significant amount of energy and leave large carbon footprints. Due to its increasingly high-demand global market and motivation to utilize newly discovered shale gas resources, the production method has been shifting to the catalytic dehydrogenation of alkanes including ethane (C_2H_6) and propane (C_3H_8). Several commercial catalytic dehydrogenation processes have been developed, e.g., the Oleflex process by UOP, and the steam active reforming (STAR) process by Uhde [1]. Both previously mentioned processes employed supported Pt-based catalysts under operating temperatures and pressures at 525–705 °C, 0.1–0.3 MPa, and 500–600 °C, 0.6–0.9 MPa, respectively. Although Pt-based catalysts exhibit excellent activity for the catalytic dehydrogenation of ethane and propane, they suffer from rapid deactivation due to unavoidable coke formation onto the catalysts. The Oleflex process has to regenerate the deactivated catalysts every 5–10 days, while the STAR process shows severe catalyst deactivation within 7 h of time on stream (TOS). Furthermore, the regeneration process is typically operated in an oxidative environment and at higher temperatures than 500–600 °C, which may lead to the sintering of Pt nanoparticles, decreasing the lifetime of catalysts. Therefore, rapid deactivation and regeneration of catalysts are the major concerns for commercial catalytic dehydrogenation processes. To overcome these concerns, the development of coke-resistant catalysts and obtaining insights into the coke formation mechanisms are highly desired [2–6].

When the thickness of a supported metal is reduced to the atomic thin structure, the support has been found to play a substantial role in catalytic properties [7, 8]. It has been, however, challenging to understand the interaction between the support and the first metal layer and relate the effect of support to adsorptive and electronic properties that significantly impact the catalytic performance. The challenges lie in the difficulties in constructing metal species with atomic precision and selecting appropriate probe reactions that are sensitive to the adsorption capability of catalysts. The performance of alkane dehydrogenation catalysts, including the activity, selectivity, and stability, is known to be sensitive to the adsorptive and electronic properties of the active sites [9–11]. For instance, Linic et al. reported that silica supported Pt_1Sn_1 nanoparticles delivered stable

Address correspondence to Zhenhua Zeng, zeng46@purdue.edu; Yang Xiao, yxiao@latech.edu; Yue Wu, yuewu@iastate.edu

propylene selectivity at thermodynamically limited conversion levels [12]. Similarly, Hook and Celik reported that the post-transition metal alloys exhibit lower binding energies of carbonaceous species and thus coke-resistant property was primarily due to the electronic effects rather than geometric effects [13]. These advances suggest that noble metal-based alloy nanoparticles can satisfactorily perform the dehydrogenation chemistry, but their working principles are still under debate. The main challenges are the coexistence of geometric (ensemble) and electronic effects on a checkerboard surface, leading to the complexity in evaluating the two coupled effects independently and the difficulty in relating the adsorptive and electronic properties of catalysts to their performance.

Herein, we show that an atomically thin Pt nanolayer, with a single atomic layer thickness, supported on a two-dimensional molybdenum titanium carbide (MXene), decouples the electronic and geometric effects in selective dehydrogenation of ethane and propane. The nanolayer catalyst has large Pt ensembles that are similar to Pt nanoparticles. As compared with Pt nanoparticles, the Pt nanolayer structure exhibits different electronic properties, leading to superior performance for catalytic dehydrogenation of ethane and propane toward ethylene and propylene. *In-situ* spectroscopic and microscopic characterizations, combined with kinetic and theoretical studies, demonstrate that the improved catalytic performance results from weakened surface adsorption and tuned electronic structure of active sites.

2 Experimental

Molybdenum powder (Mo, 1–5 μm, 99%), $Pt(NH_3)_4(NO_3)_2$ (99.995%), and hydrofluoric acid (48%) were purchased from Sigma-Aldrich, USA. Aluminum powder (Al, 325 mesh, 99%), titanium powder (Ti, 325 mesh, 99%), graphite powder (C, 7–11 μm, 99%), and boron nitride (BN, 97+%) were purchased from Alfa Aesar, USA. All the chemicals were used as received without further purification. The Mo_2TiAlC_2 powder was firstly synthesized by spark plasma sintering (SPS) of Mo/Ti/Al/C. Commercial powders of molybdenum, titanium, aluminum, and graphite were mixed in a molar ratio of 2:1:1.1:1.9. The mixture was transferred into a graphite die coated with BN. Then, the die was loaded into a Fuji-211lx SPS system and sintered at 1450 °C for 1 h under a pressure of 30 MPa. The obtained bulk Mo_2TiAlC_2 was then pulverized in a synthetic sapphire mortar and sieved through a 325-mesh screen. For the synthesis of Mo_2TiC_2 MXene, 1.0 g of the obtained Mo_2TiAlC_2 was slowly added to 10 mL of hydrofluoric acid (48%). The mixture was stirred for 72 h at 55 °C in a high-density polyethylene centrifugal tube. The resulting MXene was collected by centrifugation at 8900 rpm, after which the MXene was rinsed with distilled water and ethanol until the pH value reached 5–6. The Mo_2TiC_2 MXene powders were collected and then dried under vacuum at ambient temperature. For the synthesis of the catalyst, 0.040 g of $Pt(NH_3)_4(NO_3)_2$ was dissolved in 1 mL of deionized water (DI) to prepare a solution of 20 mg Pt per mL. Pt was loaded on Mo_2TiC_2 supports via incipient-wetness impregnation method. After the impregnation of Pt, the materials were dried overnight in vacuum at ambient temperature.

The X-ray absorption measurements were conducted at the Pt LIII edge (11.5640 keV) on the bending magnet beam line of the Materials Research Collaborative Access Team (MRCAT) at Sector 10 in the Advanced Photon Source, Argonne National Laboratory. The ionization chambers were optimized for the maximum current with linear response of 10% absorption in the incident ion chamber and 70% absorption in the transmission detector. A third detector in series simultaneously collected a Pt metal foil reference spectrum with each measurement for energy calibration. Solid samples were pressed into a cylindrical sample holder consisting of six wells, forming a self-supporting wafer. The sample holder was placed in a quartz reactor tube sealed with Kapton windows by two Ultra–Torr fittings through which gas could be flowed. The $Pt/Mo_2TiC_2T_x$ catalyst was heated to 550 °C in 3.5% H_2 for 30 min, then cooled to room temperature and flushed with He before the scan. Athena was used for energy calibration, background subtraction, and normalization of the X-ray absorption spectroscopy (XAS) data [14]. The extended X-ray absorption fine structure (EXAFS) data were fitted by Artemis to determine the coordination number (CN), bond distance (R), energy shift (ΔE_o), and Debye Waller factor ($\Delta\sigma^2$). The k range for the Fourier transform of the Pt K edge was Δk = 3–11 Å^{-1}, and the R range for the fitting was ΔR = 1.0–3.2 Å. The amplitude reduction factor (S_0^2 = 0.80) was determined by the standard Pt foil and CN, bond distances and Debye–Waller factor were adjusted from an initial structural model until a good fit was obtained. High-angle annular dark-field scanning transmission electron microscopy (HAADF-STEM) experiments were carried out on a Titan Themis scanning transmission electron microscope equipped with a Super-X energy-dispersive X-ray spectroscopy (EDX) detector.

The low-temperature H_2 chemisorption uptakes were measured by loading 100 mg of the catalyst into a U-shaped quartz reactor, which was controlled at −196, −126, −59, −38, −27, and 0 °C, respectively. When the catalyst was fully saturated at 0 °C, the reactor was then heated to 600 °C at 10 °C/min in 20 cm^3/min of He. H_2 desorption was measured at 100, 200, 300, 400, 500, and 600 °C. H_2 coverages at various temperatures were calculated by normalizing the corresponding H_2 uptakes to the saturated H_2 adsorption. The catalytic performance tests of propane and ethane dehydrogenation were carried out in a quartz-constructed fixed-bed reactor with I.D. = 0.5 in. Prior to a test, and the packed catalyst was activated in 10% H_2 (balanced with high purity N_2) at 450 °C and 100 std cc/min for 2 h. The reactor was then purged by N_2 at 50 std cc/min for 15 min. Different gas hourly space velocity (GHSV) values were achieved by varying the packed amount of catalysts and feed flow rates. The standard operating conditions were 550 °C, 10% C_3H_8 (or C_2H_6) + 89% N_2 + 1% Ar, 200 cc/min total flow rate, and 100–200 mg catalyst. The absence of mass transfer limitations, including both internal and external diffusion, was confirmed by satisfying the Weisz and Prater criterion [15], while the Mears criterion [16] was used to exclude heat transfer effects. A gas chromatography (GC) (Agilent GC6890) with both flame ionization detector (FID) and thermal conductivity detector (TCD), equipped with a Carboxen 1010 PLOT capillary column (30 m × 0.53 mm) was used for quantitative analysis of products. In typical cases, following an initial transient period, the catalyst exhibited stable performance. Unless stated otherwise, all data sets were taken at 10 min TOS during the stable period. A blank test of the MXene support with no Pt loading was carried out under standard operating conditions, with the ethane and propane conversion always less than 0.03%. All experiments have carbon mass balances of 96.2% ± 0.5%. For the reaction experiments, good repeatability generally within less than 1.9% deviation was achieved for all quantitative analyses.

Density functional theory (DFT) calculations were performed on the MXene-Pt system using the Vienna *Ab initio* Simulation Package (VASP) [17], employing the projector augmented wave method [18] for ionic cores and the PW91 exchange-correlation functional in the generalized-gradient approximation [19]. The plane-wave cutoff energy levels for bulk and slab calculations were set as 520 and 400 eV, respectively, while a first-order Methfessel–Paxton smearing with a width of 0.15 eV was

evaluated by extrapolating to zero broadening. The energy convergence criteria for all self-consistent field calculations were set as 10^{-5} eV, and all structural relaxations were performed until forces were less than 0.02 eV/Å. For structural optimization of a single unit cell of the MXene monolayer, a 12 × 12 × 1 gamma centered *k*-point mesh was used. For larger unit cells consisting of 8 × 8 unit cells of the MXene monolayer and Pt film or nanoparticles, we used a 2 × 2 × 1 *k*-point mesh in our calculations. A vacuum separation of more than 20 Å was kept on top of the MXene layer to prevent interaction with its periodic image. A Pt layer was inserted into two $Mo_2TiC_2T_x$ layers to represent our Pt/$Mo_2TiC_2T_x$ catalyst. The climbing-image nudged elastic band method was used to locate the structures of transition states (TSs) in the reactions. A p(4 × 4) Pt (111) unit cell was used for propane dehydrogenation. Each transition state was confirmed to have only one imaginary vibrational mode by vibrational normal mode analysis. All free energies were zero-point energy (ZPE)-corrected, and the change in entropies for adsorption processes was calculated by considering the temperature of the reactions in our experiments.

3 Results and discussion

In catalysis science, metal–support interaction is typically discussed in two aspects: electronic effects due to electronic perturbations at the interface of metal/support, and geometric effects related to variations in metal nanoparticle shape or crystallographic structure. However, geometric and electronic effects are not completely independent phenomena. For example, the change in metal particle size results in the change of the electron bandwidth as well as the exposed surface, topology, and active sites where the reaction takes place. Therefore, it is known to the catalysis community that decoupling the electronic effect and geometric effects is challenging. Our unique Pt monolayer catalyst supported on the Mo_2TiC_2 MXene has essentially the same surface geometry as the Pt nanoparticle, which allows us to study the electronic effect solely when the geometric effect is minimal.

To investigate the monolayer Pt surface of the Mo_2TiC_2 catalyst with atomic resolution and to identify the active metal–support interface, aberration-corrected HAADF-STEM was employed. As shown in the energy dispersive X-ray spectroscopy (EDS) elemental mapping image of the catalyst (Fig. 1(a)), Pt wets the surface of Mo_2TiC_2 evenly without forming noticeable nanoparticles or segregation. HAADF-STEM image from the [0001] direction (Figs. 1(b) and 1(c)) confirmed the observation that Pt atoms preferentially occupy the hexagonal-close-packed (hcp) positions on the Mo layer, as evidenced by the rhombic patterns of Pt atoms. Due to this special configuration, the surface structure of the smooth monolayer Pt is very similar to a Pt nanoparticle surface with a size larger than 2 nm. Thus, the geometric effect contribution of Pt nanoparticles is essentially negligible and the electronic effect in this should be the major contributor to the enhanced coke-resistant property. A more detailed HAADF-STEM image viewed along the [1120] zone axis (Fig. 1(d)) confirmed the atomic ordering of Mo_2TiC_2, where a layer of Ti is sandwiched between two Mo layers. The brighter atoms with higher *Z* contrast corresponding to Pt atom revealed

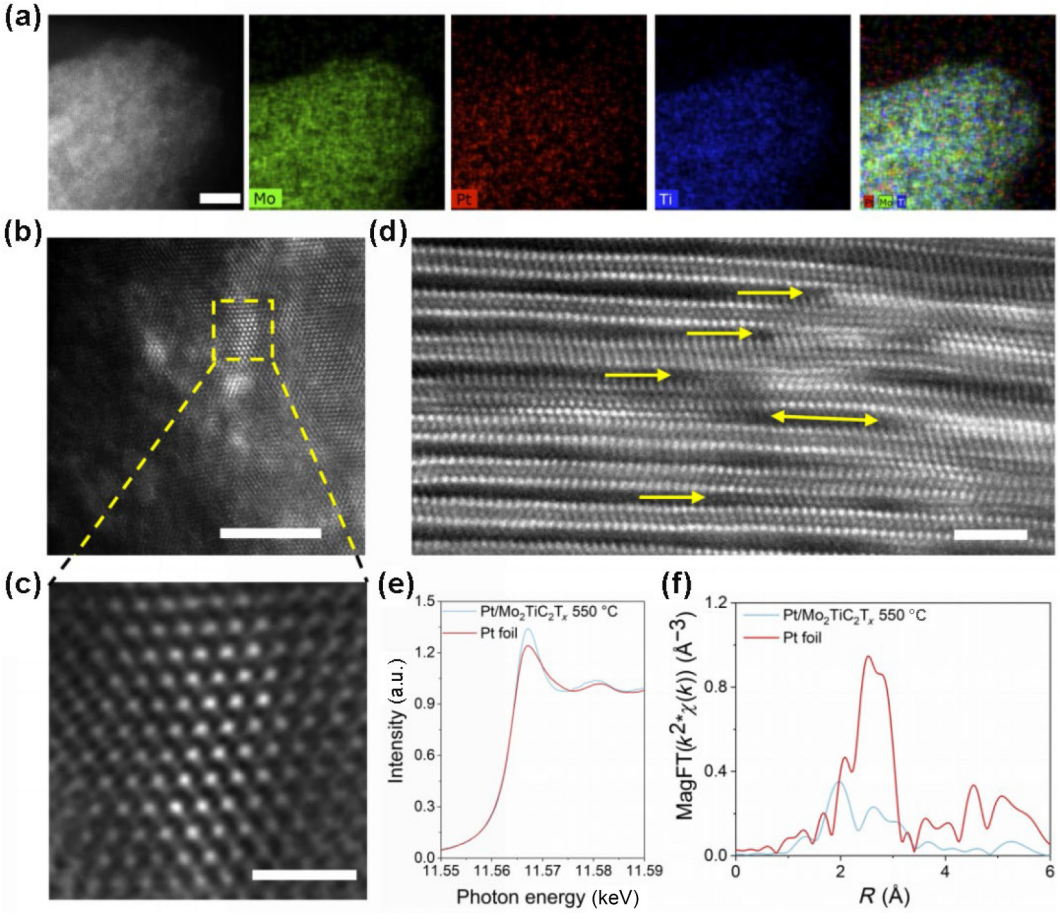

Figure 1 Structural characterization of the 0.5% Pt/$Mo_2TiC_2T_x$ catalyst reduced at 550 °C. (a) HAADF-STEM image viewing from the [0001] direction and EDS elemental mappings for Mo, Pt, Ti, and all three elements, respectively. Scale bar: 5 nm. HAADF-STEM image viewing from the [0001] direction, scale bars: (b) 5 nm and (c) 1 nm, respectively. (d) Atomic-resolution HAADF-STEM image showing metal–support interfaces, scale bar: 2 nm. (e) *In-situ* Pt L III edge XANES spectra of 0.5% Pt/$Mo_2TiC_2T_x$ reduced at 550 °C compared to Pt foil. (f) *In-situ* magnitude of the Fourier transform of the k^2-weighted EXAFS spectra of 0.5% Pt/$Mo_2TiC_2T_x$ reduced at 550 °C compared to Pt foil.

that Pt forms a monolayer intercalated between two layers of Mo_2TiC_2 MXene. This phenomenon differs from our previous observation of Pt deposited on other transition metal MXenes such as $Ti_3C_2T_x$ and $Nb_3C_2T_x$, where the MXenes alloy with Pt and form intermetallic nanoparticles [20]. This major difference indicated that the formation of monolayer Pt on MXenes is not induced by the space confinement between MXene layers, but the unique interaction between Mo layer and Pt instead. At the interface between the Pt and Mo layer of Mo_2TiC_2 MXene, it can be seen that Pt atoms deposited on the hcp positions of the Mo layer, indicating a layer-by-layer epitaxial growth of Pt on the MXene surface. These results suggest that Pt and the MXene surfaces have strong interaction. According to Wulff's theorem, the growth of Pt is determined by the metal–support bonding instead of surface energy.

The chemical environment of the Pt nanolayer on $Mo_2TiC_2T_x$ and associated electronic effect were investigated using *in-situ* XAS. Comparing the $Pt/Mo_2TiC_2T_x$ catalysts reduced at 550 °C with metallic Pt foil, Pt LIII edge X-ray absorption near edge spectra (XANES, Fig. 1(e)) show that the edge energy slightly increases from 11,564.0 to 11,564.8 eV while the whiteline intensity increases, which indicates more unoccupied Pt 5d states. The Fourier transform k^2 weighted EXAFS spectra in Fig. 1(f) show that the scattering pattern of $Pt/Mo_2TiC_2T_x$ is very different from that of the Pt foil. The peak intensity is greatly reduced at R = 2–3 Å (phase uncorrected distances), suggesting strong deconstructive interference on Pt-5d (Pt–Pt) scattering by Pt-4d (Pt–Mo) scattering [20]. Quantitative fitting of the EXAFS spectra gives the following average CNs and bond distances: 7.9 Pt–Pt bonds at 2.75 Å and 1.6 Pt–Mo bonds at 2.69 Å for the $Pt/Mo_2TiC_2T_x$ catalyst reduced at 550 °C (Table S1 and Fig. S1 in the Electronic Supplementary Material (ESM)). The results suggest that the Pt nanolayers directly bond with the Mo atoms from the MXene support, which is consistent with HAADF-STEM showing that the Pt nanolayers are in direct contact with the Mo atom layers (Figs. 1(b) and 1(c)), contributing to electronic effect of more unoccupied Pt 5d states in higher energy. All Pt/MXene catalysts in the present work were activated/reduced at high temperatures in flow H_2, which were the same operating conditions as used in our prior work. Our prior work [21] on quasi *in-situ* X-ray photoelectron spectroscopy (XPS) spectra has confirmed that the MXene surface functional groups were removed because both Mo–O peaks in the Mo 3d region and the F 1s peak disappeared as compared with the unreduced Pt/XMene catalysts.

The activity of 0.5% $Pt/Mo_2TiC_2T_x$ for ethane and propane dehydrogenation was evaluated with a continuous-flow fixed-bed reactor. Low operating pressure and high temperature give higher equilibrium conversions of both ethane and propane dehydrogenation (Fig. S2 in the ESM). Our investigations also found that relatively low operating pressure may prevent coke formation. Temperature-program surface reaction (TPSR) was used to determine the optimal reaction temperature for ethane and propane dehydrogenation (Fig. S3 in the ESM). The TPSR results show that ethane and propane cannot be activated over the Pt/Mo_2TiC_2 catalyst below about 500 °C, while the selectivity towards desired olefin products, i.e., ethane to ethylene and propane to propylene, would drop as cracking reactions (C_3H_8 to

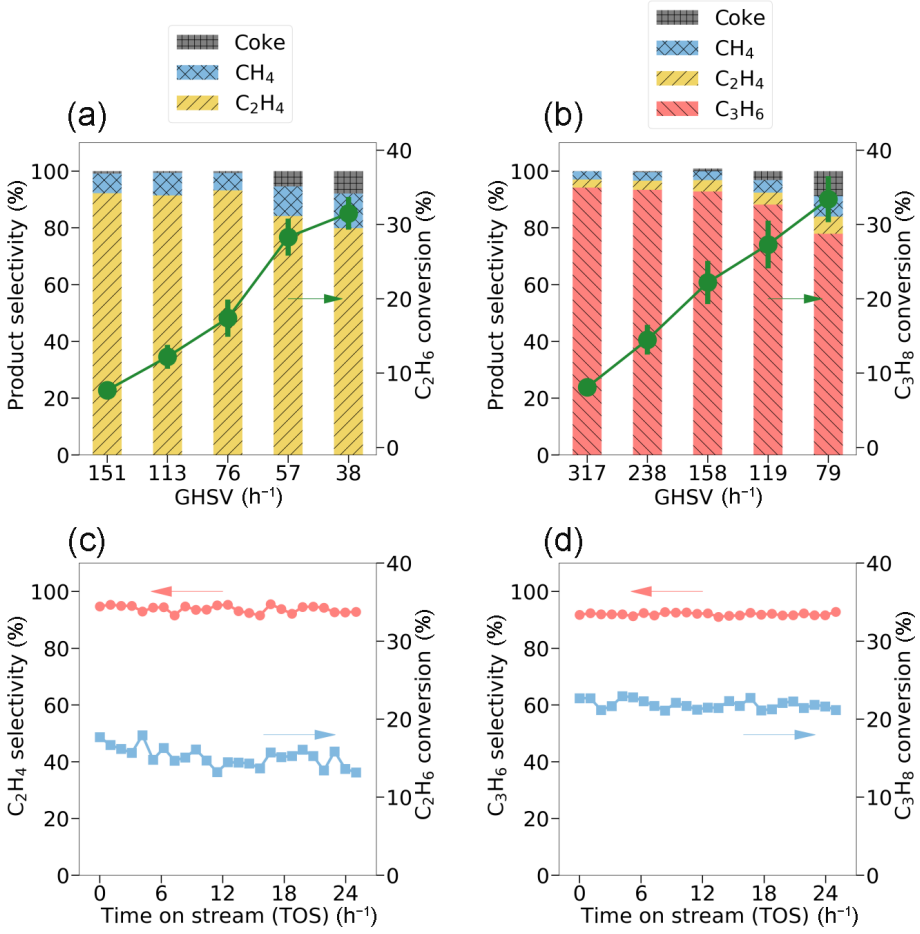

Figure 2 The catalytic performance of the 0.5% Pt/Mo_2TiC_2 catalyst for non-oxidative ethane and propane dehydrogenation. (a) Effect of GHSV on C_2H_6 dehydrogenation. (b) Effect of GHSV on C_3H_8 dehydrogenation. (c) Catalyst stability of C_2H_6 dehydrogenation. (d) Catalyst stability of C_3H_8 dehydrogenation. Operating conditions: at 550 °C, 10% C_2H_6 or 10% C_3H_8 with balanced 89% N_2 and 1% Ar as an internal standard, 200 cc/min total flow rate, 200 or 100 mg catalyst for dehydrogenation of ethane or propane, respectively.

C_2H_4 + CH_4, C_2H_6 hydrogenolysis to CH_4). Therefore, in the catalytic performance tests, the reaction temperature was 550 °C and 0.1 MPa ethane or propane partial pressure. In Figs. 2(a) and 2(b), different GHSV values were achieved by varying the weight of packed catalysts and total flow rates. Mass balances of > 95% were obtained for all reaction conditions. As shown in Fig. 2(a), the 0.5% Pt/Mo_2TiC_2 catalyst exhibited superior activity for catalytic ethane dehydrogenation with ethane conversion in the range of 8%–32% with high selectivity (80%–90%) towards ethylene. Note that when the GHSV was less than 57 h^{-1}, 5%–10% of coke was observed, indicating rapid deactivation. The main by-product of ethane dehydrogenation over the 0.5% Pt/Mo_2TiC_2 catalyst was methane (CH_4), which was formed by hydrogenolysis with *in situ* hydrogen from ethane dehydrogenation, i.e., C_2H_6 + H_2 = 2CH_4. Similarly, catalytic dehydrogenation of propane showed the same trend of propane conversion vs. GHSV (Fig. 2(b)). Coke was observed at a higher starting GHSV (119 h^{-1}), while the selectivity towards propylene was typically in the range of 78%–95%. Remarkably, both reactions showed long-term stability, i.e., no observable deactivation with 24 h TOS with more than 95% selectivity at ~ 15% ethane conversion (Fig. 2(c)) and 22% propane conversion (Fig. 2(d)), respectively. Temperature-programmed oxidation (TPO) of the 24 h spent Pt/MXene and 2 h spent Pt/SiO_2 catalysts (Fig. S4 in the ESM) shows that there is much less coke accumulation over Pt/MXene (22 mg/g_{cat} for C_2H_6 dehydrogenation, and 36 mg/g_{cat} for C_3H_8 dehydrogenation) than Pt/SiO_2 (51 mg/$_{gcat}$ for C_2H_6 dehydrogenation, and 102 mg/$_{gcat}$ for C_3H_8 dehydrogenation). It was found in our prior study that the XANES energy of the fresh Pt/SiO_2 catalyst was 11,564.0 eV [22]. The fresh Pt/SiO_2 catalyst has an average Pt particle size of ~ 2–3 nm as measured by transmission electron microscopy (TEM) scans (Fig. S5 in the ESM). The XRD patterns exhibited small peaks of the (111) and (200) planes at 39.2° and 45.6°, respectively (Fig. S6 in the ESM), which is due to the relatively small Pt particle size (~ 2 nm) [23]. For the spent Pt/SiO_2 catalyst, however, both (111) and (200) peaks were stronger, which was likely due to the aggregation of Pt particles as measured by TEM in Fig. S5 in the ESM. Both the fresh and spent Pt/MXene catalysts exhibited various peaks in XRD patterns, including (002) at 9.1°, (004) at 18.3°, (006) at 26.4°, (011) at 34.2°, (012) at 36.4°, (013) at 37.2°, (014) at 39.4°, (015) at 41.5°, (017) at 48.5°, and (010) at 59.1°, indicating excellent stability of Pt/MXene catalysts.

Both mass and heat transfer limitations were excluded prior to the measurement of reaction kinetics of ethane and propane dehydrogenation. A broader temperature range was investigated for the measurement of intrinsic kinetics in a differential reactor (conversion < 15%) at 475–575 °C for ethane and 490–570 °C for propane. Both ethane and propane dehydrogenation reactions are the 1st order (Fig. S7 in the ESM), with activation energies of 164 and 162 kJ·mol^{-1}, respectively, which is consistent with Refs. [24, 25]. These reaction rates were normalized by exposed surface Pt atoms, which were determined by Pt dispersion via the H_2-O_2 titration method, leading to turnover frequencies (TOFs). Pt dispersion refers to the ratio of surface Pt atoms to total Pt atoms. The Pt dispersion was > 98%, indicating an atomically dispersed nanolayer structure shown in Fig. 1. Note that Pt dispersion was also measured by H_2 chemisorption and CO chemisorption (see Table S2 in the ESM). As compared with the H_2-O_2 titration measurement, our results show that the dispersion values measured by H_2 chemisorption and CO chemisorption measurements vary by only −5% to 4%. TOFs of ethane and propane dehydrogenation were plotted in Fig. 3(a). TOFs of

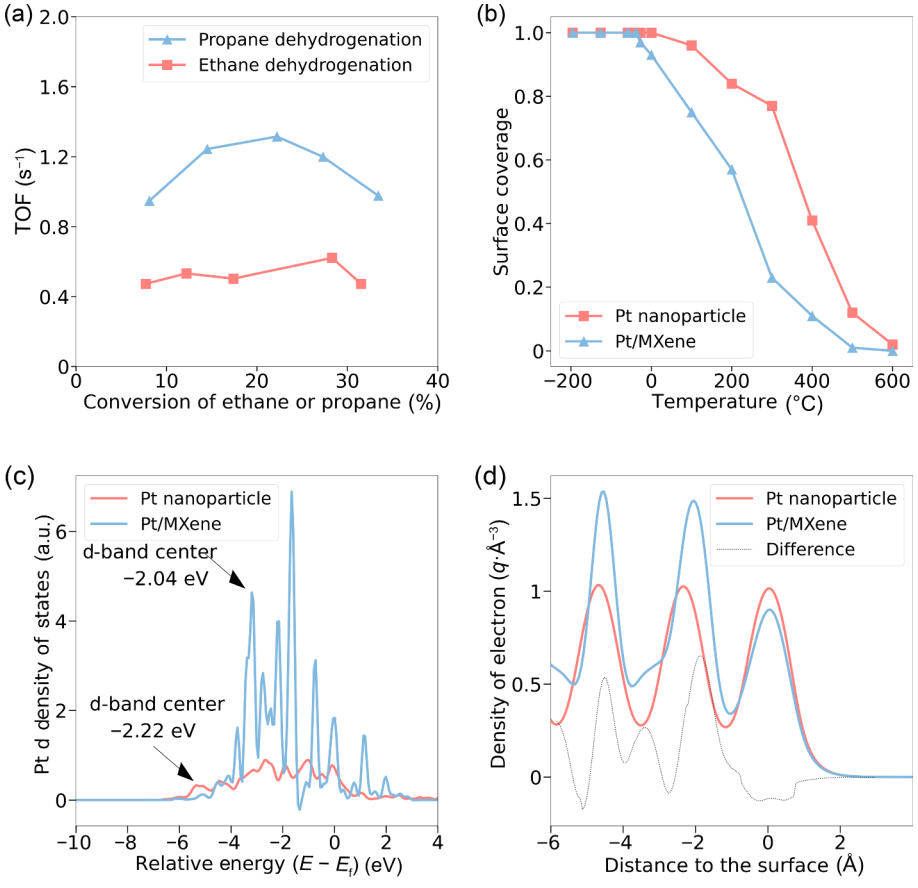

Figure 3 Electronic effects of Pt/MXene catalysts for ethane and propane dehydrogenation. (a) TOFs at various GHSV over the 0.5% Pt/MXene catalyst for ethane and propane dehydrogenation at 200 cc/min total flow rate (10% C_3H_8: 100 mg catalyst; 50% C_3H_8: 200 mg catalyst; 90% C_3H_8: 300 mg catalyst). (b) Surface coverage at various temperatures for Pt nanoparticle and Pt MXene catalysts. (c) Pt d density of states of Pt MXene and Pt nanoparticle catalysts. (d) A comparison of the electron density profile of the Pt nanoparticle and Pt/$Mo_2TiC_2T_x$ surface.

ethane dehydrogenation fell in 0.4–0.7 s^{-1}, while TOFs of propane dehydrogenation were in between 0.9 to 1.2 s^{-1}. It suggests that although GHSVs were varied in a broad range (38–151 h^{-1} for ethane, and 79–317 h^{-1} for propane), the reaction rates per surface Pt atom were essentially constant for both ethane and propane. It further demonstrates surface Pt atoms were the active sites for both ethane and propane dehydrogenation.

The low-temperature H_2 chemisorption was used to further study the coke-resistant property of the catalyst. Hydrogen surface coverage was evaluated from −196 to 600 °C for Pt nanoparticle and Pt/Mo_2TiC_2, respectively, as shown in Fig. 3(b). The surface coverage of Pt nanoparticles exceeded that of Pt/Mo_2TiC_2 when the temperature was higher than 100 °C, indicating weaker hydrogen adsorption over Pt/Mo_2TiC_2. The Pt/Mo_2TiC_2 catalyst exhibited high activity, i.e., 0.5–2.0 s^{-1} TOF (Fig. 3(c)) and had a similar surface structure to that of Pt nanoparticles greater than about 2 nm, which implies that the more unoccupied 5d states of Pt nanolayer play a critical role in controlling the catalytic activity as well as the stability, which is further supported by the shifted d-band centers in density of states (DOSs) (Fig. 3(c)). The d-band center theory [26] claims that the binding energy of a molecule and the electronic structure of a metallic or alloy catalyst can be well associated with the d-band center energy. We calculated that the d-band center energy of the Pt nanoparticle is −2.22 eV, which is consistent with literature reports. For the Pt/MXene catalyst, the d-band center energy is calculated as −2.08 eV, which indicates electron transfer from the Pt surface layer to the MXene support, leading to a less negatively charged surface. Furthermore, the charge density difference plot propane adsorption over Pt nanoparticle and Pt/MXene catalysts also verify that the Pt/MXene surface is more positively charged, which is likely a cause of weaker adsorption. The charge density profiles (the *y*-axis of Fig. 3(d)) of Pt nanoparticle and Pt/$Mo_2TiC_2T_x$ as well as their difference are plotted in Fig. 3(d) with respect to the distance to the catalyst surface (the *x*-axis of Fig. 3(d)). Furthermore, the charge density differences plot between the clean surfaces and propane adsorption surfaces of both Pt nanoparticle and Pt/MXene catalysts also verifies that the Pt/MXene surface is more positively charged, which is likely a cause of weaker adsorption (Fig. S8 in the ESM). The position $x = 0$ represents the outermost Ti layer and negative values of x represents moving towards the bulk material. There is a significant decrease in the electron density of Pt bound to $Mo_2TiC_2T_x$ compared to Pt nanoparticle. Moreover, there is a higher minimum in the electron density between Pt and $Mo_2TiC_2T_x$ than that between Pt nanoparticle and its adjacent Pt layer (near $x = -1$ Å), signifying more electron sharing in the former case. Taken together, these should decrease the binding between Pt/$Mo_2TiC_2T_x$ with interfacial species in comparison with the Pt nanoparticle surface.

DFT calculations were used to investigate the reaction pathways and energy changes of propane dehydrogenation to different products, including dehydrogenative and cracking products. The structures of reaction intermediates and transition states are illustrated in Fig. 4, with the free energies of the different reaction pathways. The dehydrogenation of propane involves multiple C–H activation and dissociative adsorption of alkyl species (C_3H_7*, C_3H_6*, C_3H_5*, etc.). Our DFT calculations suggest that the scission of the first three C–H on both Pt(111) and Pt/Mo_2TiC_2 surfaces have similar free energies, with intermediates and transitional states on Pt(111) surface having slightly lower energies, which also agrees with the higher hydrogen coverage on Pt(111) surface than Pt/Mo_2TiC_2. Deep dehydrogenation (C_3H_5*

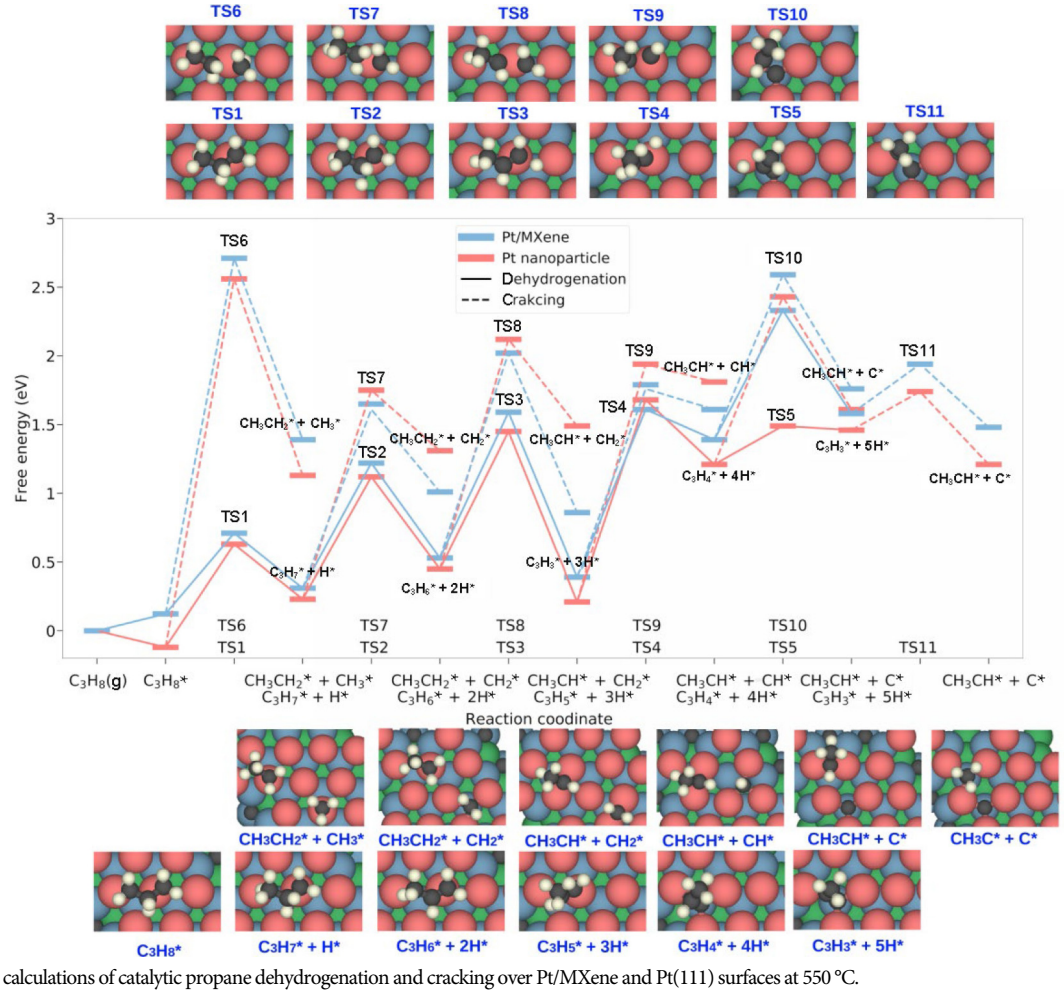

Figure 4 DFT calculations of catalytic propane dehydrogenation and cracking over Pt/MXene and Pt(111) surfaces at 550 °C.

to C_3H_4*), however, becomes unfavorable on both surfaces as the free energy of the intermediates increases significantly (more than 0.5 eV). On the Pt/Mo_2TiC_2 surface, further dehydrogenation (C_3H_4* to C_3H_3*) which eventually leads to a coking product becomes even less favorable with both increased free energy of the C_3H_3* intermediate and the larger energy barrier to overcome. In comparison, the C_3H_4* to C_3H_3* reaction on Pt(111) surface has a significantly lower energy barrier (~ 0.7 eV) than that of Pt/Mo_2TiC_2 surface, suggesting an easier path for coke formation on Pt nanoparticles. Regarding cracking reaction pathways, the free energies of the products and the transitional states are always higher than the corresponding ones of the dehydrogenation reaction, which accounts for the increased cracking products at elevated reaction temperatures. As shown in Fig. 4, Pt(111) and Pt/Mo_2TiC_2 surfaces favor cracking reactions at different stages. In general, free energy differences of the cracking intermediates, dehydrogenation intermediates, and the transitional states on Pt(111) are larger by ~ 0.5 eV than those on Pt/Mo_2TiC_2 surface, which suggests that the Pt nanoparticles should have a higher selectivity (over 90%) towards dehydrogenation than cracking. However, the Pt(111) surface favors the deep dehydrogenation, therefore eventually leading to coking and the rapid deactivation of the catalyst. The significant increase by about 0.7 eV in the energy barrier in the deep dehydrogenation reaction steps explains the excellent coke-resistant property of the Pt/Mo_2TiC_2 catalyst.

4 Conclusions

In conclusion, epitaxial growth of thin Pt nanolayers on the surface of Mo_2TiC_2 Mxene leads to strong Pt–Mo bonding at the metal–support interface, which helps anchor the Pt atoms on the MXene surface. Consequently, Pt/Mo_2TiC_2 catalysts exhibit stable conversion of ethane and propane to ethylene and propylene with high selectivity and excellent coke resistance. The unique Pt monolayer provides an opportunity to evaluate the electronic effect on the catalytic performance, as the surface structure of the Pt monolayers shares a similar surface structure with larger Pt nanoparticles, where the geometric effect can be minimized. Due to the altered electronic structures of the Pt nanolayers, the hydrogen adsorption on Pt/Mo_2TiC_2 is weaker than that on Pt nanoparticle surfaces, preventing the deep dehydrogenation which eventually leads to coking on Pt surfaces. These discoveries are important for understanding the role electronic effects play in product selectivity and catalyst stability. In addition, the metal–support interaction is dependent on the substrate and metal components, providing wide opportunities to explore high-performance MXene-supported metal catalysts, as well as reveal their structure–property relationship for broader reactions with industrial importance.

Acknowledgements

Y. W., Z. L., F. Y., and X. P. L. thank the support from Iowa State University (Herbert L. Stiles Professorship). Y. X. and T. K. M. appreciate the start-up funding from the College of Engineering and Science at Louisiana Tech University. Z. W. W. and J. T. M. were supported by the National Science Foundation under Cooperative Agreement (NSF/ERC CISTAR, No. EEC-164772). Use of the Advanced Photon Source, a US Department of Energy Office of Basic Energy Sciences, was supported under contract no. DE-AC02-06CH11357. The MRCAT beamline 10-BM is supported by the Department of Energy as well as the MRCAT member institutions.

Electronic Supplementary Material: Supplementary material (supplementary figures and tables) is available in the online version of this article at https://doi.org/10.1007/s12274-023-6022-2.

References

[1] Sattler, J. J. H. B.; Ruiz-Martinez, J.; Santillan-Jimenez, E.; Weckhuysen, B. M. Catalytic dehydrogenation of light alkanes on metals and metal oxides. *Chem. Rev.* **2014**, *114*, 10613–10653.

[2] Ye, G. H.; Wang, H. Z.; Duan, X. Z.; Sui, Z.; Zhou, X. G.; Coppens, M. O.; Yuan, W. K. Pore network modeling of catalyst deactivation by coking, from single site to particle, during propane dehydrogenation. *AIChE J.* **2019**, *65*, 140–150.

[3] Aly, M.; Fornero, E. L.; Leon-Garzon, A. R.; Galvita, V. V.; Saeys, M. Effect of boron promotion on coke formation during propane dehydrogenation over Pt/γ-Al_2O_3 catalysts. *ACS Catal.* **2020**, *10*, 5208–5216.

[4] Lian, Z.; Si, C. W.; Jan, F.; Zhi, S. K.; Li, B. Coke Deposition on Pt-based catalysts in propane direct dehydrogenation: Kinetics, suppression, and elimination. *ACS Catal.* **2021**, *11*, 9279–9292.

[5] Zhang, Y.; Wang, B. J.; Fan, M. H.; Ling, L. X.; Zhang, R. G. Ethane dehydrogenation over the g-C_3N_4 supported metal single-atom catalysts to enhance reactivity and coking-resistance ability. *Nano Res.* **2023**, *16*, 6142–6152.

[6] Thakur, R.; VahidMohammadi, A.; Smith, J.; Hoffman, M.; Moncada, J.; Beidaghi, M.; Carrero, C. A. Insights into the genesis of a selective and coke-resistant MXene-based catalyst for the dry reforming of methane. *ACS Catal.* **2020**, *10*, 5124–5134.

[7] Li, Y. Y.; Zhang, Y. S.; Qian, K.; Huang, W. X. Metal–support interactions in metal/oxide catalysts and oxide-metal interactions in oxide/metal inverse catalysts. *ACS Catal.* **2022**, *12*, 1268–1287.

[8] Pu, T. C.; Zhang, W. H.; Zhu, M. H. Engineering heterogeneous catalysis with strong metal–support interactions: Characterization, theory and manipulation. *Angew. Chem., Int. Ed.* **2023**, *62*, e202212278.

[9] Gao, X. F.; Xu, W. H.; Li, X.; Cen, J. J.; Xu, Y. Z.; Lin, L. L.; Yao, S. Y. Nonxidative dehydrogenation of propane to propene over Pt-Sn/Al_2O_3 catalysts: Identification of the nature of active site. *Chem. Eng. J.* **2022**, *443*, 136393.

[10] Chen, X. W.; Peng, M.; Xiao, D. Q.; Liu, H. Y.; Ma, D. Fully exposed metal clusters: Fabrication and application in alkane dehydrogenation. *ACS Catal.* **2022**, *12*, 12720–12743.

[11] Zhang, W.; Wang, H. Z.; Jiang, J. W.; Sui, Z.; Zhu, Y. A.; Chen, D.; Zhou, X. G. Size dependence of Pt catalysts for propane dehydrogenation: From atomically dispersed to nanoparticles. *ACS Catal.* **2020**, *10*, 12932–12942.

[12] Motagamwala, A. H.; Almallahi, R.; Wortman, J.; Igenegbai, V. O.; Linic, S. Stable and selective catalysts for propane dehydrogenation operating at thermodynamic limit. *Science* **2021**, *373*, 217–222.

[13] Hook, A.; Celik, F. E. Predicting selectivity for ethane dehydrogenation and coke formation pathways over model Pt-M surface alloys with *ab initio* and scaling methods. *J. Phys. Chem. C* **2017**, *121*, 17882–17892.

[14] Ravel, B.; Newville M. *ATHENA*, *ARTEMIS*, *HEPHAESTUS*: Data analysis for X-ray absorption spectroscopy using IFEFFIT. *J. Synchrotron Rad.* **2005**, *12*, 537–541.

[15] Weisz, P. B.; Prater, C. D. Interpretation of measurements in experimental catalysis. *Adv. Catal.* **1954**, *6*, 143–196.

[16] Mears, D. E. Diagnostic criteria for heat transport limitations in fixed bed reactors. *J. Catal.* **1971**, *20*, 127–131.

[17] Kresse, G.; Furthmüller, J. Efficiency of *ab-initio* total energy calculations for metals and semiconductors using a plane-wave basis set. *Computat. Mater. Sci.* **1996**, *6*, 15–50.

[18] Kresse, G.; Joubert D. From ultrasoft pseudopotentials to the projector augmented-wave method. *Phys. Rev. B* **1999**, *59*, 1758–1775.

[19] Perdew, J. P.; Chevary, J. A.; Vosko, S. H.; Jackson, K. A.; Pederson, M. R.; Singh, D. J.; Fiolhais, C. Atoms, molecules, solids, and surfaces: Applications of the generalized gradient approximation for exchange and correlation. *Phys. Rev. B* **1992**, *46*, 6671–6687.

[20] Li, Z.; Cui, Y. R.; Wu, Z. W.; Milligan, C.; Zhou, L.; Mitchell, G.; Xu, B.; Shi, E. Z.; Miller, J. T.; Ribeiro, F. H. et al. Reactive

Metal–support interactions at moderate temperature in two-dimensional niobium-carbide-supported platinum catalysts. *Nat. Catal.* **2018**, *1*, 349–355.

[21] Li, Z.; Xiao, Y.; Chowdhury, P. R.; Wu, Z. W.; Ma, T.; Chen, J. Z.; Wan, G.; Kim, T. H.; Jing, D. P.; He, P. L. et al. Direct methane activation by atomically thin platinum nanolayers on two-dimensional metal carbides. *Nat. Catal.* **2021**, *4*, 882–891.

[22] Li, Z.; Yu, L.; Milligan, C.; Ma, T.; Zhou, L.; Cui, Y. R.; Qi, Z. Y.; Libretto, N.; Xu, B.; Luo, J. W. et al. Two-dimensional transition metal carbides as supports for tuning the chemistry of catalytic nanoparticles. *Nat. Commun.* **2018**, *9*, 5258.

[23] Xiao, Y.; Varma, A. Highly selective nonoxidative coupling of methane over Pt-Bi bimetallic catalysts. *ACS Catal.* **2018**, *8*, 2735–2740.

[24] Frash, M. V.; Van Santen, R. A. Activation of small alkanes in Ga-exchanged zeolites: A quantum chemical study of ethane dehydrogenation. *J. Phys. Chem. A* **2000**, *104*, 2468–2475.

[25] Li, Q.; Sui, Z. J.; Zhou, X. G.; Chen, D. Kinetics of propane dehydrogenation over Pt-Sn/Al_2O_3 catalyst. *Appl. Catal. A General* **2011**, *398*, 18–26.

[26] Nørskov, J. K.; Bligaard, T.; Logadottir, A.; Bahn, S.; Hansen, L. B.; Bollinger, M.; Bengaard, H.; Hammer, B.; Sljivancanin, Z.; Mavrikakis, M. et al. Universality in heterogeneous catalysis. *J. Catal.* **2002**, *209*, 275–278.